
**Searching for diboson resonances in the
all-hadronic final state
and
a Lorentz invariance based deep neural network for
W-tagging**

Dissertation
zur
Erlangung der naturwissenschaftlichen Doktorwürde
(Dr. sc. nat.)

vorgelegt der
Mathematisch-naturwissenschaftlichen Fakultät
der
Universität Zürich

von
Thea Klaeboe Arrestad
aus
Norwegen

Promotionskommission:
Prof. Dr. Benjamin Kilminster
Prof. Dr. Florencia Canelli
Prof. Dr. Jesse Thaler
Dr. Andreas Hinzmann

Zürich 2018

Abstract

Zusammenfassung

Die vorliegende Doktorarbeit stellt blabla.....

Contents

| | |
|---|-----------|
| 1 The Standard Model and Beyond | 2 |
| 1.1 The Standard Model Lagrangian | 2 |
| 1.1.1 Particles and fields | 2 |
| 1.1.2 Electroweak theory | 2 |
| 1.1.3 The Higgs Mechanism | 2 |
| 1.1.4 Quantum Chromodynamics | 2 |
| 1.2 Beyond Standard Model Physics | 2 |
| 1.2.1 The hierarchy problem and the gravitational force | 2 |
| 1.2.2 Theories of New Physics | 2 |
| 1.2.3 Heavy Vector Triplet formalism | 2 |
| 2 Experimental setup | 3 |
| 2.1 The Large Hadron Collider | 3 |
| 2.2 The CMS detector | 5 |
| 2.2.1 Coordinate system | 6 |
| 2.2.2 Tracking detectors | 6 |
| 2.2.3 Electromagnetic calorimeter | 8 |
| 2.2.4 Hadron calorimeter | 10 |
| 2.2.5 Muon chambers | 12 |
| 2.3 Trigger system: From collision to disk | 13 |
| 3 Event reconstruction | 15 |
| 3.1 Track and primary vertex reconstruction | 15 |
| 3.2 The Particle Flow Algorithm | 15 |
| 3.3 Jet reconstruction | 15 |
| 3.3.1 Jet clustering | 15 |
| 3.3.2 Jet substructure reconstruction | 15 |
| 3.4 Monte Carlo Simulation | 15 |
| 3.4.1 Matrix Element Generators | 15 |
| 3.4.2 Shower Generators | 15 |
| 4 Diboson resonance searches in CMS | 16 |
| 4.1 Searches for heavy resonances decaying to dibosons | 16 |
| 4.2 Search I: First search for diboson resonances at 13 TeV | 16 |
| 4.3 Search II: Developing a new vector boson tagger | 16 |
| 4.4 Search III: A novel multi-dimensional search | 16 |

| | |
|---|-----------|
| 5 LoLa: A novel Machine Learning W-tagger for future analyses | 17 |
| 5.1 Machine Learning: The future of high-performance, low-latency taggers | 17 |
| 5.2 LoLa: A Lorentz Invariance Based Deep Neural Network for W-tagging | 17 |
| 5.2.1 Inputs | 17 |
| 5.2.2 The Combination Layer | 17 |
| 5.2.3 The Lorentz Layer | 17 |
| 5.3 Decorrelating from mass and p_T | 17 |
| 5.4 Performance | 17 |
| 6 Summary | 18 |
| Bibliography | 19 |

Introduction

A short explanation of NP decaying to dibosons (Vprime, Gravition), jets in the boosted regime (substructure), the search strategy of 2015+2016 (1D) and 2017 (3D). Touch on triboson signatures to emphasise 3D

1 The Standard Model and Beyond

1.1 The Standard Model Lagrangian

1.1.1 Particles and fields

1.1.2 Electroweak theory

1.1.3 The Higgs Mechanism

1.1.4 Quantum Chromodynamics

1.2 Beyond Standard Model Physics

1.2.1 The hierarchy problem and the gravitational force

1.2.2 Theories of New Physics

Warped extra dimensions

Compositeness

1.2.3 Heavy Vector Triplet formalism

2 Experimental setup

2.1 The Large Hadron Collider

In March 1984, the European Organization for Nuclear Research CERN) and the European Committee for Future Accelerators (ECFA) held a workshop in Lausanne entitled "Large Hadron Collider in the LEP Tunnel". This is history's first written mention of the Large Hadron Collider (LHC) and the topic under discussion was exactly how and where to build a new type of high-energy collider, capable of bringing hadrons to collide rather than leptons. The LHC would be housed in a tunnel which, at the time, was under excavation to host the Large Electron-Positron Collider (LEP) designed to collide leptons with center-of-mass energies up to around 200 GeV. LEP was a circular collider with a circumference of 27 km and the tunnel hosting it was located roughly 100 meters underground on the border between France and Switzerland, at the outskirts of Geneva. The justification for building a machine like the LHC, was that once LEP got to maximum reach, a new and more powerful collider would be needed in its place in order to probe higher energies. While collisions of electrons with positrons provided exceptionally clean and precise measurements due to them being point particles, their lightness prevent them from being accelerated to higher energies. Collisions of hadrons, however, would allow for center-of-mass energies two orders of magnitude higher than that of LEP. Therefore, after running a while at two times the W mass (160 GeV) and reaching a maximum center-of-mass energy of 209 GeV, LEP was dismantled in 2000 in order to make room for the LHC.

The Large Hadron Collider started up in September 2008 and, while having the same 27-kilometer radius as the LEP collider, is capable of accelerating protons up to a center-of-mass energy of around 14 TeV, 70 times that of LEP. The accelerator consists of two oppositely going proton beams, isolated from each other and under ultrahigh vacuum, which are accelerated up to speeds close to that of the speed of light through radio frequency (RF) cavities, before being brought to collide at four different interaction points along the ring. These four collision points correspond to the location of the four LHC particle detectors; ATLAS, CMS, LHCb and ALICE. While ATLAS and CMS are general-purpose detectors built in order to study a large range of different physics processes, LHCb and ALICE are built for dedicated purposes; LHCb for b-physics processes and ALICE for heavy ion collision. A protons journey from gas to one of the LHC collision points is as follows: First, hydrogen nuclei are extracted from a small tank of compressed hydrogen gas and stripped of their electrons. The remaining protons are then injected into the LINAC2, a linear accelerator responsible for increasing the proton energy to about 50 MeV through RF cavities that push charged particles forward by switching from positive to negative electric fields. LINAC2 additionally divides the constant stream of particles into equally spaced "bunches" by careful tuning of the frequency of the field switch. The accelerated protons are then injected into the Proton Synchrotron Booster (PSB), where their energy is increased thirty folds more, to an energy of roughly 1.4 GeV. The two final acceleration stages before the protons reach the LHC ring are the Proton Synchrotron and Super Proton Synchrotron, eventually leaving the

protons with a total energy of 450 GeV. The protons are now ready for the final stage of their travel and are injected into the two beam pipes of the LHC in oppositely going direction. They are injected in trains of 144 bunches each (with an order of 10^{11} protons per bunch), where each bunch is roughly 7.5 meters apart (or 25 ns). There are some larger beam gaps present in each beam in order to give the beam dump and injection kickers sufficient time to reach full voltage, where the largest one, the beam abort gap, is roughly 3 ms or 900 m long. The ring is filled with proton bunches until these are equally distributed throughout the two rings, a process taking roughly 4 minutes. This is called a "fill". Here, the protons are accelerated to their maximum energy of 6.5 TeV, a process taking roughly 20 minutes, through eight RF cavities. These RF cavities are also responsible of keeping the proton bunches tightly bunched, ensuring maximum luminosity at the four collision points. A complete sketch of the CERN accelerator complex is shown in Figure 2.1.

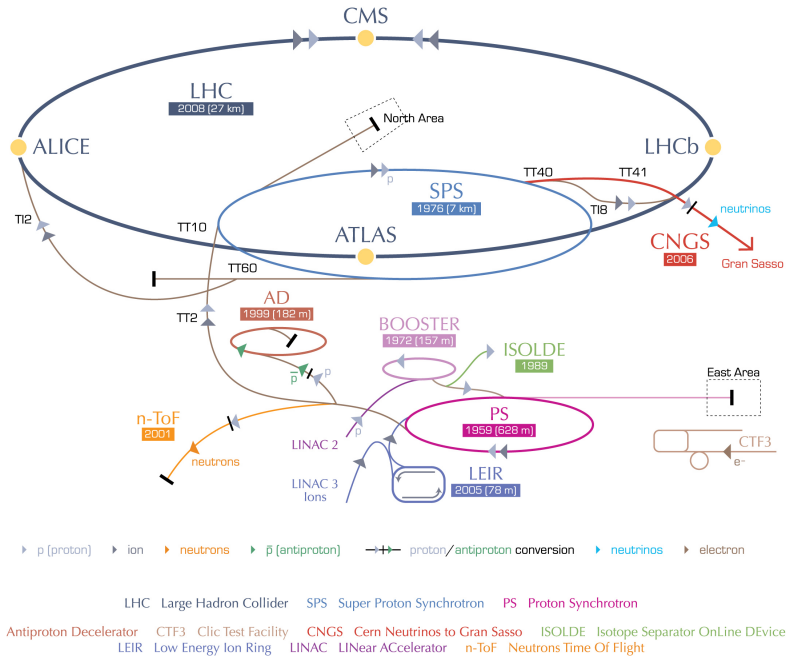


Figure 2.1: The Large Hadron Collider accelerator complex. The four collision points along the ring correspond to the location of the LHC particle detectors CMS, LHCb, ATLAS and ALICE [1].

After the beams have reached their maximum energy and are stably circulating in the LHC ring, they are brought to collide. The goal of such a collision, which occurs every 25 nano seconds, is that some of the protons will undergo an inelastic collision, allowing the quark/gluon constituents of each proton to interact with one another and produce new and interesting particles. The number of times such an interaction will take place inside a detector per area and time is quantified through the luminosity, \mathcal{L} , which is the proportionality factor between the number of observable events per second, and the cross section σ of the process you are interested in

$$\frac{dN_{events}}{dt} = \mathcal{L}\sigma. \quad (2.1)$$

The cross section is the probability that an event (like one which would produce new and interesting particles) will occur and is measured in barns, where 1 barn = 10^{-28} m². This proportionality factor should therefore be as high as possible. It depends only on parameters of the detector and can, in the case of LHC, be defined through the following accelerator quantities

$$\mathcal{L} = \frac{N_b^2 n_b f_{rev} \gamma_r}{4\pi \epsilon_n \beta_*} F, \quad (2.2)$$

where N_b is the number of particles per bunch, n_b is the number of bunches, f_{rev} is their revolution frequency, γ_r is the relativistic gamma factor, ϵ_n is the transverse beam emittance (how confined the particles are in space and momentum), β_* is the beta function at the collision point (how narrow, or "squeezed", the beam is) and F is a reduction factor to account for a constellation where the beams do not collide heads-on but at slight crossing angles. From this, it becomes clear that the main goal of the LHC is to; maximize the number of particles (N_b, n_b), their frequency (f_{rev}) and their energy (γ_r), while at the same time ensuring the protons are packed together as tightly as possible (lower ϵ_n and β_*). Using the nominal values of the LHC, the peak luminosity is roughly $\mathcal{L} \sim 10^{34} \text{ cm}^{-2} \text{ s}^{-1}$.

The peak luminosity of the LHC by the end of Run 2 in 2018 was grazing around $2.0 \cdot 10^{34} \text{ cm}^{-2} \text{ s}^{-1}$, corresponding to 2 times the nominal design luminosity.

To quantify the size and statistical power of a given LHC dataset, the integrated luminosity is used. This is the integral of the instantaneous luminosity over time and is defined as

$$\mathcal{L}_{int} = \int \mathcal{L} dt. \quad (2.3)$$

It is usually defined in units of inverse cross section, b⁻¹.

Despite the LHC starting up in 2008, there would be another year before data taking began. In March 2010, the LHC saw its first collision with a center-of-mass energy of 7 TeV, and continued running at this energy collecting around 5 inverse femtobarns of data by the end of 2011. In 2012, the energy was increased to 8 TeV and the LHC continued running until a planned long shutdown scheduled to begin in February 2013, collecting a total of $\sim 20 \text{ fb}^{-1}$ and discovering the Higgs boson. This marked the end of Run 1 and the beginning of a two-year maintenance project intended to prepare the LHC for running at a center-of-mass energy of 13 TeV; Run 2.

Run 2, and where this thesis begins, started in June 2015. With the accelerator now running at 90% of its nominal energy, and with a peak luminosity between 1-2 times the design luminosity, the LHC managed to collect an impressive $\sim 160 \text{ fb}^{-1}$ at this energy until its planned shutdown at the end of 2018. Some key LHC accelerator parameters that were in use for the datasets analyzed in this thesis, are quoted in Table 2.1

2.2 The CMS detector

The Compact Muon Solenoid (CMS) detector is true to its name; with a diameter of 15 meters and a weight of 14000 tons, it is 60 % smaller but two times heavier than its general purpose counterpart, the ATLAS detector. Its large weight is due to the CMS housing the world's largest and most powerful solenoid: A superconducting niobium titanium coil circulating 18500 Amps and capable of generating a magnetic field of 3.8 Tesla. Together with its corresponding iron return yoke, responsible for reflecting the escaping magnetic flux, it accounts for 90% of the total detector weight. The CMS detector is cylindrically symmetric and organized in the following way: closest to the beam pipe and at a radius of about 3

| Parameter | Units | Nominal | 2015 | 2016 | 2017 |
|-------------------------|---|---------|------|------|----------|
| Energy | [TeV] | 7.0 | 6.5 | 6.5 | 6.5 |
| Bunch spacing | [ns] | 25 | 25 | 25 | 25 |
| Bunch intensity | $\times 10^{11}$ [protons/bunch] | 1.15 | 1.15 | 1.15 | 1.2-1.45 |
| Bunches per train | | 144 | 144 | 96 | 144 |
| Total number of bunches | | 2808 | 2244 | 2220 | 2556 |
| β^* | [cm] | 55 | 80 | 40 | 27/25 |
| Peak luminosity | $\times 10^{34}[\text{cm}^{-2}\text{s}^{-1}]$ | 1.0 | 0.5 | 1.4 | 2.0 |
| Integrated luminosity | | | 4.2 | 39.7 | 50.2 |

Table 2.1: Some key LHC detector parameters achieved during the first years of 13 TeV data taking

cm, the inner tracking system begins. It consists of an inner silicon pixel detector and an outer silicon strip tracker, stretching out to a radius of roughly 1.2 meters. Following the tracker are two calorimeter layers: the electromagnetic calorimeter (ECAL) consisting of lead tungstate scintillating crystals and responsible for measuring the energy of electromagnetically interacting particles, followed by the hermetic hadronic calorimeter (HCAL) measuring the energy of hadrons. Contrary to "standard" configurations for general purpose detectors, the CMS calorimeters are located inside the superconducting solenoid. This allows the detector to be rather compact, by reducing the necessary radius of the calorimeters, and additionally for the magnet to be strong enough (the magnetic field strength depends on the coil radius) to allow muon detectors to be located within the magnetic field so their momentum can be measured. The muon detectors are alternated with three layers of steel return yoke responsible for containing and reflecting the magnetic field and which only allows muons and weakly interacting particles to pass. A schematic overview of the CMS detector is shown in Figure 2.2. In the following, the different sub-detectors will be described in detail.

2.2.1 Coordinate system

To describe locations within the CMS detector, a Euclidian space coordinate system is used. Here, the positive z axis points along the beam pipe towards the west, the positive x axis points towards the center of the LHC ring, and the positive y axis upw towards the earths surface. Due to the cylindrical symmetry of the detector, polar coordinates are more convenient and most frequently encountered. In this scheme, the azimuthal angle ϕ is measured in the xy-plane, where $\phi = 0$ correspond to the positive x axis and $\phi = \pi/2$ correspond to the positive y axis. The polar angle θ is measured with respect to the z axis, $\theta = 0$ aligning with the positive and $\theta = \pi$ with the negative z axis. To define a particles angle with respect to the beam line, the pseudorapidity $\eta = -\ln \tan(\theta/2)$ is preferred over θ . This is due to the fact that particle production is approximately constant as a function of pseudorapidity and, more importantly, because differences in pseudorapidity are Lorentz invariant under boosts along the z-axis when assuming massless particles. To measure angular difference between particles in the detector, the variable $R = \sqrt{\eta^2 + \phi^2}$ is used, again Lorentz invariant under longitudinal boosts. A summary of the CMS coordinate system together with some example values are shown in Figure 2.3.

2.2.2 Tracking detectors

The CMS tracker is responsible for accurately reconstructing the momentum of charged particles and consists of two sub-detectors. Closest to the interaction point, and where the

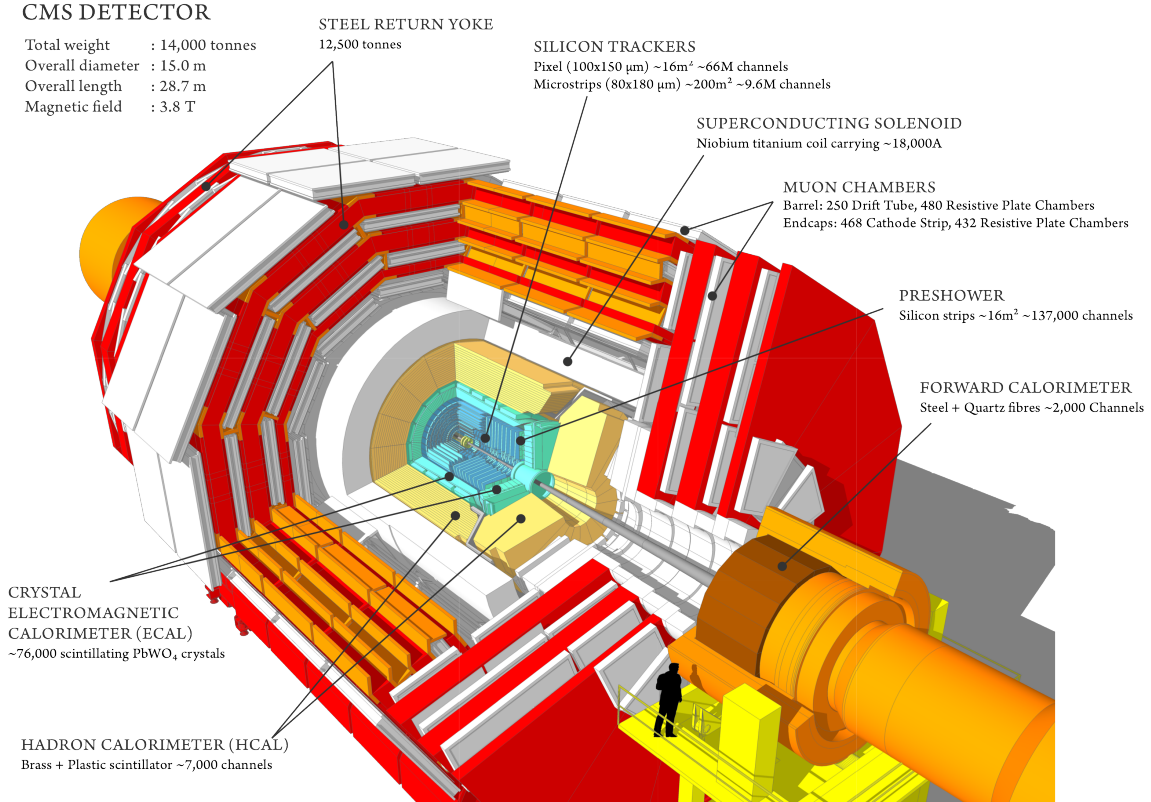


Figure 2.2: The CMS detector and its subsystems: The silicon tracker, electromagnetic and hadron calorimeters, the superconducting solenoid and the muon chambers inter-layered with the steel return yoke [2].

particle intensity is the highest, the silicon pixel detector is located. Upgraded in 2017, from the so-called Phase-0 to the Phase-1 layout, it is structured in four cylindrical barrel layers at radii 2.9, 6.8, 10.9 and 16.0 cm (the barrel pixel) and three disks in each of the forward regions placed at a distance from the nominal interaction point of 29.1, 39.6 and 51.6 cm (the forward pixel). A sketch of the current Phase-I pixel detector compared to the Phase-0 detector is shown in Figure 2.4. The sensors located closest to the beam pipe are subject to hit intensities of $\mathcal{O}(\text{MHz}/\text{mm}^2)$ which puts strict constraints on the maximum sensor size in order to minimize occupancy in the detector. The pixel sensors are $100 \mu\text{m} \times 150 \mu\text{m}$ with a thickness of $285 \mu\text{m}$, and when counting both barrel and pixel sensors, sum up to a total of 79 million. The pixel sensors are mounted on detector modules with 16 read-out chips each, where the type of read-out chip depends on how close the module is to the beam pipe: the inner layer uses read-out chips with a rate capability of $600 \text{ MHz}/\text{cm}^2$ while for the outer layers, read-out chips with a rate capability of up to $200 \text{ MHz}/\text{cm}^2$ are sufficient.

As the hit intensity reduces as you go further away from the beam pipe, the pixel sensors are replaced by silicon strip sensors, making up the second of the two tracker sub-systems, the silicon strip tracker. There are ten strip layers in total, stretching out to a radius of roughly 130 cm. These are divided into four sections: The inner barrel (TIB) with four strip layers, the two inner endcaps (TID) consisting of three disks each, the outer barrel (TOB) consisting of 6 cylindrical layers and the two endcaps (TEC) with 9 strip layers each. A schematic overview of the strip tracker layout is shown in Figure 2.5. The strips in the TIB and TID are 10 cm long, with a width of $80 \mu\text{m}$ and a thickness of $320 \mu\text{m}$. The TOB and TEC sections consist of slightly larger strips of $25 \text{ cm} \times 180 \mu\text{m}$ and a thickness of $500 \mu\text{m}$. The strip

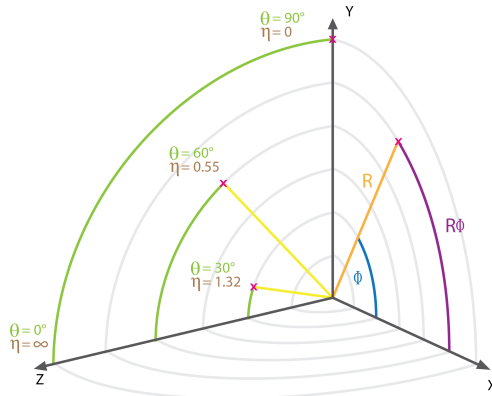


Figure 2.3: The CMS coordinate system [3]

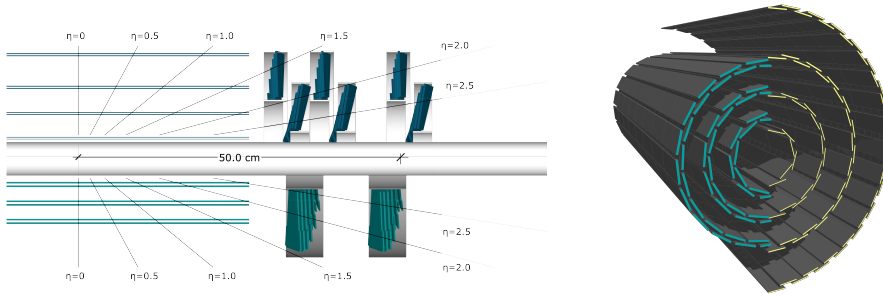


Figure 2.4: Left: The forward pixel detector layout before (bottom) and after (top) the Phase-I upgrade. Right: The barrel pixel detector before (left) and after (right) the Phase-I upgrade [4].

tracker has a total of 10 million detector strips and covers an area of $\sim 200 \text{ m}^2$. To prolong the silicon detector lifetime, the entire tracker (pixel and strip) is kept at a temperature of -20°C through a liquid cooling system. The tracker has a coverage up to $|\eta| < 2.6$ and a resolution of roughly $\sigma/p_T \approx 1.5 \times 10^{-5} p_T + 0.005$.

2.2.3 Electromagnetic calorimeter

Following the tracking detectors is the electromagnetic crystal calorimeter (ECAL). Consisting of 75 848 laterally segmented scintillating lead tungstate (PbWO_4) crystals, it was designed to have the highest possible photon energy and position resolution in order to resolve a Higgs boson decaying into two photons, the cleanest of the Higgs discovery channels. With a goal of a photon/electron energy resolution of 0.5% above 100 GeV, the choice of detector material for the ECAL has been its most crucial design feature. In order to withstand the high doses of radiation and the high magnetic field present within the detector, while at the same time generating well-defined signal responses within the 25 nanoseconds between particle collisions, an extremely dense and transparent material capable of producing fast and clean photon bursts when hit, is required. The choice eventually fell on metal-heavy lead tungstate crystals, each taking roughly two days to artificially grow (and a total of about ten years to grow all of them). With a density of $\delta = 8.28 \text{ g/cm}^3$ (slightly higher than for stainless steel), the crystals are compact enough to yield excellent performance without taking up too much volume, allowing the ECAL to sit within the CMS superconducting solenoid. The homogeneous medium allows for a better energy resolution as it minimizes sampling

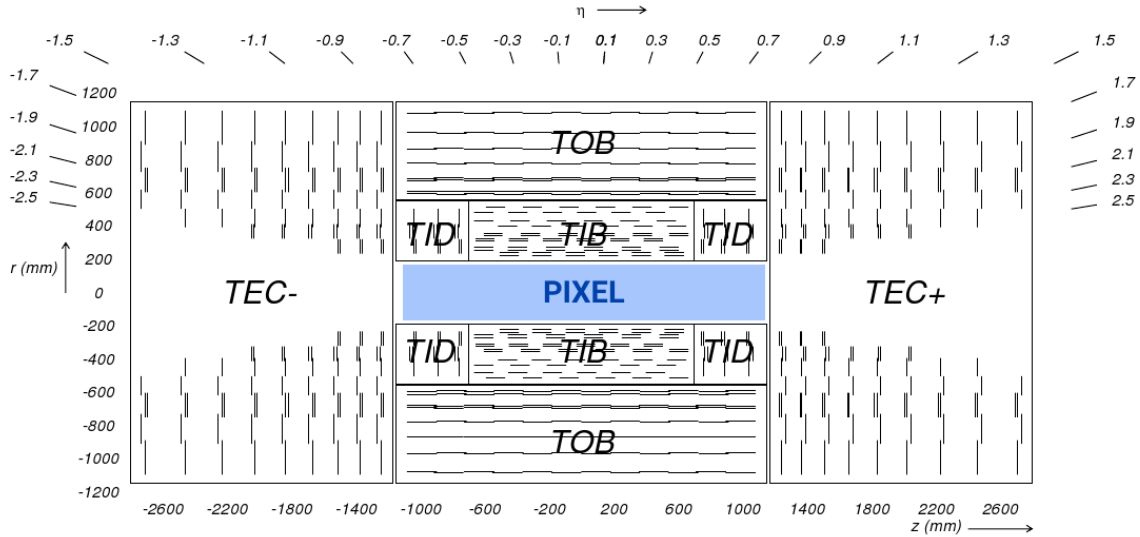


Figure 2.5: Schematic of the CMS silicon strip tracker and its four subsections: The inner barrel (TIB), inner endcaps (TID), the outer barrel (TOB) and the two endcaps (TEC) [5].

fluctuation effects and it additionally contains enough oxygen in crystalline form to make it highly transparent to their entire scintillation emission spectrum. With an extremely short radiation length and small Moliére radius ($X_0 = 0.85$ cm,

$$R_M = 2.19$$

cm), the required homogeneity, granularity and compactness is obtained while at the same time emitting 80% of generated light within the 25 ns timeframe required. The largest drawbacks with a lead tungstate detector is the low light yield (100 γ per MeV), requiring dedicated avalanche photodiodes to increase the gain, as well as a light yield which strongly depends on the temperature. The detector response to an incident electron changes by 3.8 ± 0.4 % per degree Celsius which requires the ECAL temperature to be kept stable around $18.180(5)$ °C, obtained through an intricate water cooling system. The ECAL is completely hermetic and sorted into a barrel part (EB), covering pseudorapidities up to $|\eta| < 1.48$, and two endcap parts (EE) extending the total coverage to $|\eta| < 3.0$ in order to match the tracker coverage of $|\eta| < 2.5$. In order to improve the γ/π_0 separation power, a pre-shower detector (ES) using lead absorbers and silicon sensors covers the forward region between $1.65 < |\eta| < 2.6$. The crystals in the barrel are organized into supermodules, each consisting of about 1700 crystals, while the endcap is divided into two half disks consisting of 3662 crystals each (so-called "Dees"). Each PbWO₄ crystal weighs around 1.5 kilogram and has a slightly tapered shape with a front face of 2.2×2.2 cm² in the barrel and 2.86×2.86 cm² in the endcaps. The crystals are 2.3 and 2.2 cm long in the barrel and endcaps, respectively. The total volume of the calorimeter including barrel and endcaps is 11 m² and weighs a total of 92 tons. The ECAL detector layout is illustrated in Figure 2.6.

Having no longitudinal segmentation, the ECAL relies on an accurate reconstruction of the event primary vertex, provided by the tracker, in order to reconstruct the photon angle correctly.

The obtained energy resolution of the ECAL can be parametrized in three parts: a stochastic, a noise and a constant term [6]. It is given as

$$\frac{\sigma E}{E} = \frac{2.8\%}{\sqrt{E}} \oplus \frac{0.128 \text{ GeV}}{E} \oplus 0.3\%$$

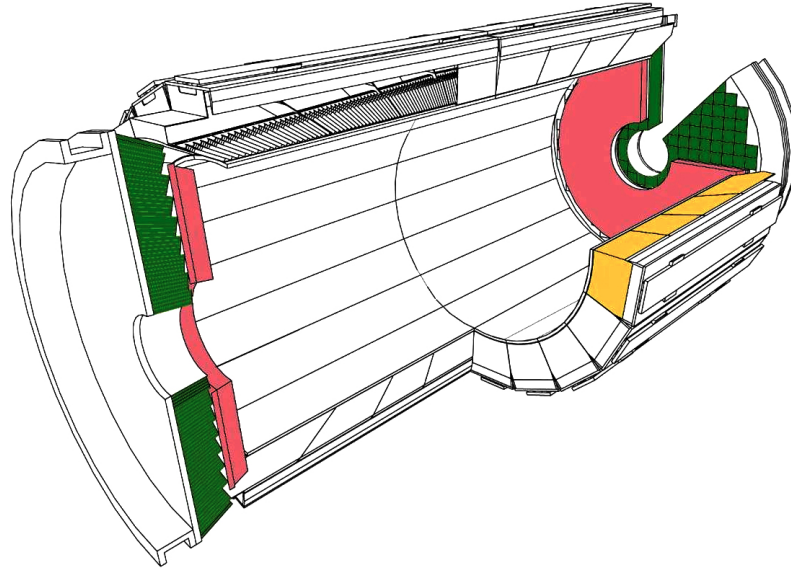


Figure 2.6: A schematic of the CMS electromagnetic calorimeter showing the barrel supermodules (yellow), the individual barrel crystals (black,top left), the endcap modules (green) and the pre-shower detectors (pink) [5].

where the constant values were estimated in an electron test beam. The constant term of 0.3% is dominated by the non-uniformity in longitudinal light collection [7], and one of the main goals of the detector design was to get this term below 1%. The energy resolution as a function of electron energy is shown in Figure 2.7.

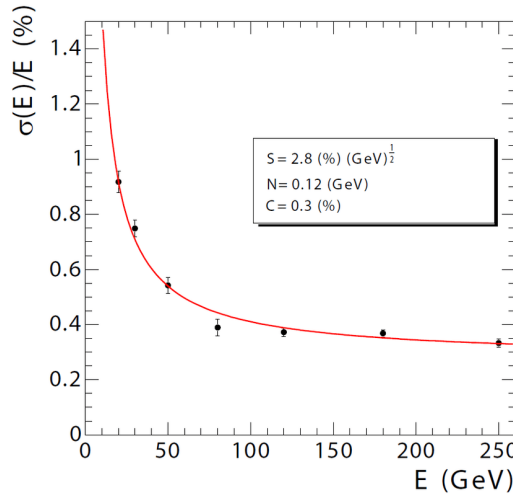


Figure 2.7: The ECAL energy resolution as a function of electron energy as measured in an electron test beam. [6]

2.2.4 Hadron calorimeter

Outside the crystal calorimeter is the hadron calorimeter (HCAL). It is the combined response of the ECAL and the HCAL that are responsible for measuring the energy of quarks, gluons and neutrinos through the reconstruction of particle jet energy and missing transverse energy.

The HCAL is a sampling calorimeter, meaning it consists of alternating layers of dense brass absorber material and plastic scintillators. When a particle hits an absorber plate, it interacts with the absorber material and generates a shower of secondary particles which themselves generate new particle showers. These particles then generate light in the scintillating material which is proportional to their energy, and summing up the total amount of generated light over consecutive layers within a region, called a "tower", is representative of the initial particles energy. The hadron calorimeter is split into four regions: the inner (HB) and outer (HO) barrel, the endcap (HE) and the forward region (HF). A schematic of the CMS HCAL is shown in Figure 2.8.

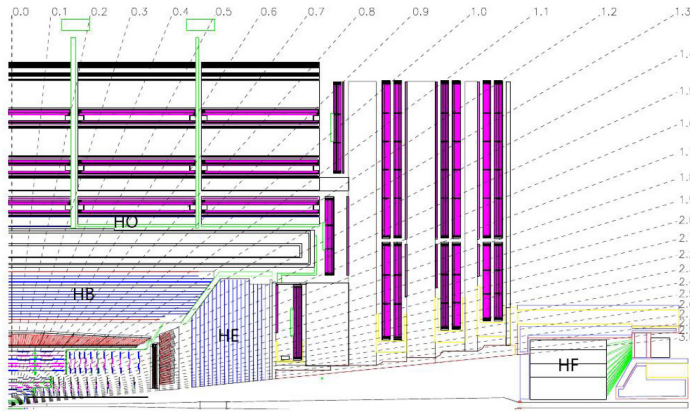


Figure 2.8: The four regions of the CMS hadron calorimeter: the inner (HB) and outer (HO) barrel, the endcap (HE) and the forward region (HF) [5]

The inner barrel lies within the superconducting solenoid volume and covers the pseudorapidity range $|\eta| < 1.3$. It consists of 36 identical wedges, each of which weighing 26 tonnes, split into two half barrels (HB+ and HB-). A photograph of the wedges taken during installation is shown in Figure 2.9.



Figure 2.9: The installation of the barrel HCAL wedges consisting of alternating layers of brass absorber plates and plastic scintillator, each weighing roughly 26 tonnes [8].

The wedges are made up of flat brass absorber plates oriented parallel to the beam axis.

These plates consist of a 4 cm thick front steel plate followed by eight 5 cm thick brass plates, six 5.6 cm thick brass plates and ending with a 7.5 cm thick steel back plate. The absorber plates are then alternated by 4 mm thick plastic scintillator tiles, the detectors active medium, which are read out using wavelength-shifting plastic fibers. The effective thickness of the barrel hadron calorimeter in terms of interaction lengths increases with the polar angle θ , starting out at about $5.8 \lambda_I$ at an angle of 90 degrees, and increases to $10.6 \lambda_I$ at $|\eta| < 1.3$. As the energy resolution of the calorimeter depends on how much of the particles shower can be absorbed by the calorimeter, the quality of the energy measurement depends on its thickness. Due to the CMS design, the HB is confined to the volume between the ECAL (ending at a radius of 1.77 m) and the magnetic coil (starting at a radius of 2.95 m). In the central η region, the combined ECAL and HCAL interaction length is too small to sufficiently contain hadron showers. In order to ensure adequate sampling, especially of late starting showers, an additional layer of scintillator has therefore been added outside of the solenoid coil. This is the outer barrel (HO). It uses the coil itself as absorbing material and increases the total barrel calorimeter interaction length to $11.8 \lambda_I$. The hadron calorimeter endcaps (HE) are located in the forward region close to the beam pipe and covers the pseudorapidity range $1.3 < |\eta| < 3.0$, a region containing about 35 % of the particles produced in collisions. Due to its close proximity to the beam pipe, the endcaps need to handle extremely high rates as well as have a high radiation tolerance. As the resolution in the endcap region anyways is limited by pile-up and magnetic field effects, the hadron calorimeter endcaps were designed to minimize the cracks between HB and HE rather than having the best single-particle resolution (as is the case for the barrel). The absorber plates in the endcaps are mounted in a staggered geometry rather than on top of each other as is done in the barrel, in order to contain no dead material and provide a hermetic self-supporting construction. In order to obtain a completely hermetic calorimeter, an additional hadron forward calorimeter (HF) is added in the very forward region. Stretching out to a pseudorapidity of $|\eta| = 5.2$, this detector is located so close to the beam pipe that the particle rate exceeds 10^{11} per cm^2 , receiving roughly 760 GeV per proton-proton collision compared to an average of 100 GeV for the rest of the detector. It consists of a cylindrical steel structure with an outer radius of 130 cm and inner radius of 12.5 cm, located 11.2 meters from the interaction points. Also a sampling calorimeter, it consists of grooved 5 mm thick steel absorber plates, where the quartz fiber active medium is inserted into these grooves. The energy resolution of the CMS ECAL and HCAL for pions is measured in a test beam as a function of energy and is shown in Figure 2.11.

The inclusion of the HO increases the resolution by 10 % for a pion energy of 300 GeV. The final energy resolution parametrization when using ECal+HB+HO is given by a stochastic and a constant term, as for ECAL, and is

$$\frac{\sigma E}{E} = \frac{84.7\%}{\sqrt{E}} \oplus 7.4\%.$$

2.2.5 Muon chambers

The outer part of the CMS detector is dedicated to performing muon identification, momentum measurement and triggering. In order to do so, the muon system is made up of three types of gaseous particle detectors: drift tube (DT) chambers, cathode strip chambers (CSCs) and resistive plate chambers (RPCs), all integrated into the magnetic return yoke structure. In the barrel region, where particle rates are low and the magnetic field uniform, DT chambers are used and cover the pseudorapidity region $|\eta| < 1.2$. In the endcap regions, however, the muon rates and background levels are considerably higher and the magnetic field itself is

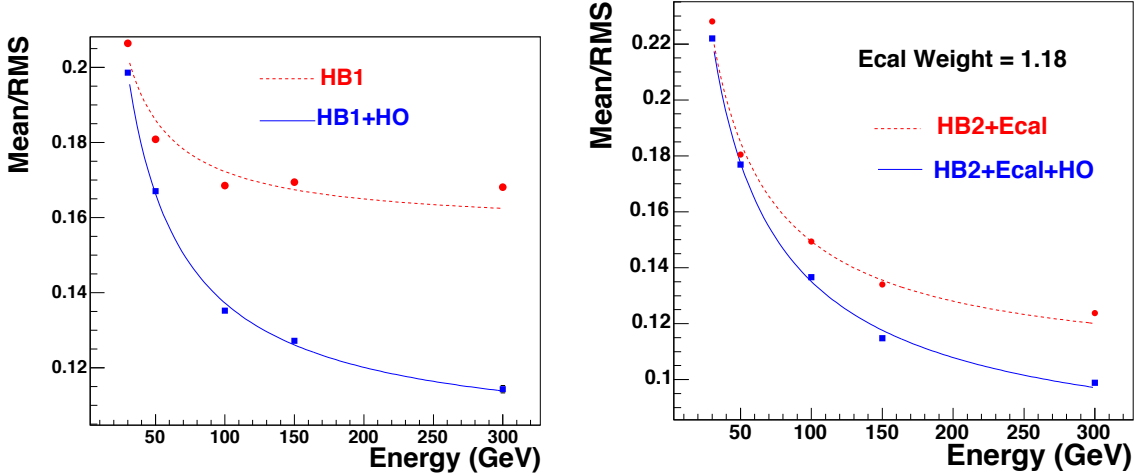


Figure 2.10: The calorimeter energy resolution as a function of pion energy using the HB only or HB+HO (left) and when adding ECal and HCal measurements (right) [9].

large and non-uniform. Here; faster, finer segmented and more radiation hard CSCs are used, covering the region $0.9 < |\eta| < 2.4$. To ensure accurate muon triggering, a complimentary dedicated muon triggering system has been added both in the barrel and in the endcaps. Made out of RPCs, they provide an excellent time resolution at a sharp p_T threshold and cover the region $|\eta| < 1.6$. These chambers also assist in resolving ambiguities if multiple hits are present within a DT/CS chamber. A schematic overview of the muon system is shown in

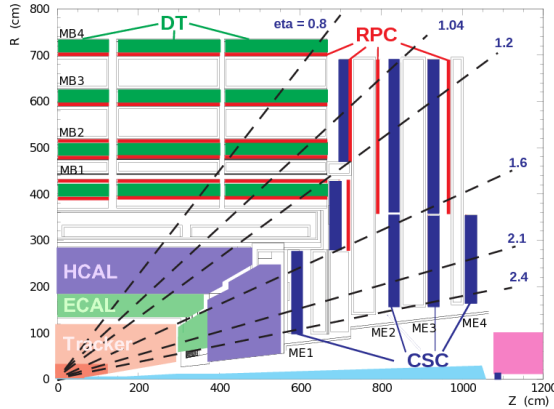


Figure 2.11: A schematic overview of the muon chambers: the DT chambers in the barrel, the CSCs in the endcaps and the redundant RPC system stretching out to $|\eta| < 1.6$ and used for triggering purposes [?].

2.3 Trigger system: From collision to disk

With protons in CMS colliding at a rate of 40 MHz, there are only 25 nanoseconds between collisions available to process event data. One billion collisions take place every second, and with an event size of roughly 1 MB, it is impossible for all of these events to be read out and stored to disk. The CMS triggering system is therefore designed to make ultra fast high-quality decisions of which events are interesting and which events are not. The first stage of triggering, called Level 1 (L1), is designed to reduce the event rate to a maximum of

100 kHz through custom-designed hardware. It uses coarse data from the muons system and calorimeters in order to make a decision on whether the event should be recorded or not, a decision that needs to happen within 3.2 micro seconds. In the mean time, the full granularity data is stored in detector front-end electronics awaiting the L1 decision. The information used by L1 is gathered in three steps. First, trigger primitives are created. For the muon system, these consist of track segments from each of the three types of muon detectors. For the calorimeter, trigger primitives are generated by calculating the transverse energy of a trigger tower (energy deposits with an $\eta - \phi$ coverage of 0.087×0.087) and assigning it to the correct bunch crossing. Trigger primitives from the calorimeter information is then passed on to a regional trigger which defines electron, muon and jet candidates. Some of this information is passed to the muon trigger (is particle a minimum ionizing particle?). The muon trigger combines the track information with the calorimeter information and selects a maximum of four muon candidates and calculates their momentum, position, charge and quality. This is done in the global muon trigger. The output from the regional calorimeter trigger is also passed to a global calorimeter trigger which provides information about the jets, total transverse energy and missing energy in the event. Combining the information from the global muon trigger and the global calorimeter trigger, the L1 decides whether to keep the event or not by combining several decisions by simple logic operations (AND/OR/NOT) to form up to 128 algorithms.

If the events is accepted, the full event information is read out at a rate of 100 kHz and passed to the so-called "event filter farm", a single processor farm made out of commodity computers. Here, the full precision of the detector data is used on order to take decisions based on offline-quality reconstruction algorithms. The goal of the HLT is to eventually reduce the event rate to an average rate of 400 Hz for offline event storage.

3 Event reconstruction

3.1 Track and primary vertex reconstruction

The CMS tracker gets traversed by *bigO* 1000 charged particles at each bunch crossing, produced by an average of roughly 34 proton-proton interactions happening simultaneously. This makes track reconstructions extremely challenging, and is the reason why a high granularity of the tracker is vital. Track reconstruction describes the process of taking hits from the pixel and strip detectors, combining them and estimating the momentum and flight direction of the charged particle responsible for producing the hits. It is an extremely computationally heavy process and is based on what is called a combinatorial Kalman filter [?]. A Kalman filter is an algorithm that uses time-dependent observations in order to estimate unknown variables, by proceeding progressively from one measurement to the next, improving the knowledge of the trajectory with each new measurement. The track reconstruction software in CMS (called the Combinatorial Track Finder (CTF)) constructs its collection of tracks by iteratively looping over the hits and reconstructing tracks, then removing those which are already used as inputs for a previous track. It starts from a seed in the inner most tracker layers, usually two or three hits, and then extrapolates the seed trajectories searching for additional hits to associate to that candidate. It then disregards tracks that fail certain criteria based on a χ^2 calculation taking both hit and trajectory uncertainties into account, as well as the number of missing hits. The track reconstruction algorithm is effective over the full tracker coverage range up to $|\eta| < 2.5$ and can reconstruct particles with momenta as low as 0.1 GeV or particles which are produced up to 60 cm from the beam line. In the central region, particles with a momentum of 100 GeV have a p_T -resolution of roughly 2.8 %, a transverse impact parameter resolution of 10 μm and a longitudinal impact parameter of 30 μm .

In order to define the location and uncertainty of every proton-proton interaction in an event, primary-vertex reconstruction is performed. Primary vertices lie within a radius of a few millimeters of the beam axis and are defined as the common origin of groups of tracks. The reconstruction algorithm takes as input the reconstructed tracks from the previous step which pass certain selection criteria, clusters the tracks that share a common origin and then fit for the position of each vertex. Each track must have at least 2 hits in the pixel layers and no less than 5 hits in the pixel+strip as well as a $\chi^2 < 20$ from a fit to the particle trajectory to be considered as input for the vertex finder. The primary vertex resolution is around 12 μm in x and 10 μm in z for vertices with at least 50 tracks.

Offline, all events are required to have at least one primary vertex reconstructed within a 24 cm window along the beam axis, with a transverse distance from the nominal interaction region of less than 2 cm. The reconstructed vertex with the largest value of summed physics object p_T^2 is selected as the primary interaction vertex where the hard scattering process occurred.

3.2 The Particle Flow Algorithm

3.3 Pile-up removal

3.4 Jet reconstruction

3.4.1 Jet clustering

3.4.2 Jet substructure reconstruction

Grooming

N-subjettiness

3.5 Monte Carlo Simulation

3.5.1 Matrix Element Generators

3.5.2 Shower Generators

4 Diboson resonance searches in CMS

- 4.1 Searches for heavy resonances decaying to dibosons**
- 4.2 Search I: First search for diboson resonances at 13 TeV**
- 4.3 Search II: Developing a new vector boson tagger**
- 4.4 Search III: A novel multi-dimensional search**

5 LoLa: A novel Machine Learning W-tagger for future analyses

5.1 Machine Learning: The future of high-performance, low-latency taggers

5.2 LoLa: A Lorentz Invariance Based Deep Neural Network for W-tagging

5.2.1 Inputs

5.2.2 The Combination Layer

5.2.3 The Lorentz Layer

5.3 Decorrelating from mass and p_T

5.4 Performance

6 Summary

Bibliography

- [1] CERN, “Accelerators and Schedules”, 2018 (accessed November 12, 2018),
<https://beams.web.cern.ch/content/accelerators-schedules>.
- [2] CMS, “CMS Detector Design”, 2018 (accessed November 21, 2018),
<https://cms.cern/news/cms-detector-design>.
- [3] T. Lenzi, “Development and Study of Different Muon Track Reconstruction Algorithms for the Level-1 Trigger for the CMS Muon Upgrade with GEM Detectors”, Master’s thesis, U. Brussels (main), 2013.
- [4] A. Dominguez et al., “CMS Technical Design Report for the Pixel Detector Upgrade”, Technical Report CERN-LHCC-2012-016. CMS-TDR-11, CERN, Sep, 2012.
- [5] CMS Collaboration, “The CMS Experiment at the CERN LHC”, *JINST* **3** (2008) S08004, doi:10.1088/1748-0221/3/08/S08004.
- [6] P. Adzic et al., “Energy resolution of the barrel of the CMS electromagnetic calorimeter”, *JINST* **2** (2007) P04004, doi:10.1088/1748-0221/2/04/P04004.
- [7] C. Biino, “The CMS Electromagnetic Calorimeter: overview, lessons learned during Run 1 and future projections”, *Journal of Physics: Conference Series* **587** (2015), no. 1, 012001.
- [8] L. V. . EP, “Assembly of the 7th wedge. Assemblage du 7eme module”, (Aug, 2000). CMS Collection.
- [9] S. Sharma, “Understanding the performance of CMS calorimeter”, *Pramana* **69** (Dec, 2007) 1069–1074, doi:10.1007/s12043-007-0229-8.